

UnRectDepthNet: Self-Supervised Monocular Depth Estimation using a Generic Framework for Handling Common Camera Distortion Models

Varun Ravi Kumar^{1,4}, Senthil Yogamani², Markus Bach¹,
Christian Witt¹, Stefan Milz^{3,4} and Patrick Mäder⁴

¹Valeo DAR Kronach, Germany ²Valeo Vision Systems, Ireland

³Spleenlab GmbH, Germany ⁴Technische Universität Ilmenau, Germany

Abstract—In classical computer vision, rectification is an integral part of multi-view depth estimation. It typically includes epipolar rectification and lens distortion correction. This process simplifies the depth estimation significantly, and thus it has been adopted in CNN approaches. However, rectification has several side effects, including a reduced field-of-view (FOV), resampling distortion, and sensitivity to calibration errors. The effects are particularly pronounced in case of significant distortion (e.g., wide-angle fisheye cameras). In this paper, we propose a generic scale-aware self-supervised pipeline for estimating depth, euclidean distance, and visual odometry from unrectified monocular videos. We demonstrate a similar level of precision on the unrectified KITTI dataset with barrel distortion comparable to the rectified KITTI dataset. The intuition being that the rectification step can be implicitly absorbed within the CNN model, which learns the distortion model without increasing complexity. Our approach does not suffer from a reduced field of view and avoids computational costs for rectification at inference time. To further illustrate the general applicability of the proposed framework, we apply it to wide-angle fisheye cameras with 190° horizontal field-of-view (FOV). The training framework *UnRectDepthNet* takes in the camera distortion model as an argument and adapts projection and unprojection functions accordingly. The proposed algorithm is evaluated further on the KITTI dataset, and we achieve state-of-the-art results that improve upon our previous work *FisheyeDistanceNet* [1]. Qualitative results on a distorted test scene video indicate excellent performance¹.

I. INTRODUCTION

Depth estimation is a crucial task for automated driving. Stereo cameras were primarily used in automotive for computing depth. Some of the initial prototypes of automated driving relied primarily on depth estimation [2]. Multi-view geometric approaches were traditionally used for computing depth. CNN models have been dominant with supervised learning in various visual perception tasks. In the case of depth estimation, self-supervised learning has enabled high accuracy in depth estimation [3], [4], [5], [6], [7]. There is also a trend of integrating depth estimation task in multi-task models [8], [9], [10]. Most of the depth estimation methods were demonstrated in the context of automated driving on rectified KITTI video sequences where barrel distortion was removed.

Rectification is a fundamental step in dense depth estimation [11]. In the case of stereo cameras, epipolar rectification is performed to enable matching only in one direction along

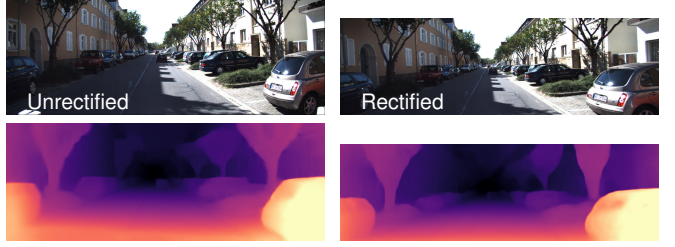


Fig. 1 Depth obtained from a single unrectified (left) and rectified KITTI image (right) respectively. Our scale-aware model, UnRectDepthNet, yields precise boundaries, fine depth maps.

the horizontal scanline. This approach can also be extended to monocular cameras by using two consecutive frames giving rise to motion stereo. These rectification steps also require the removal of non-linear distortion. Although it is convenient to work with rectilinear projections, there are practical issues that arise due to rectification, which are discussed in detail in Section II. Rectification has also been transferred to CNN based approaches as an inductive bias to simplify the learning. Yadati *et al.* [12] demonstrates that CNN based two-view depth estimation is challenging without rectification and attempts to solve it in a simpler setting. To the best of our knowledge, all the methods reported on KITTI make use of the barrel distortion corrected images. Automotive cameras like fisheye surround-view cameras exhibit a strong distortion, and it is not easy to rectify them. Recently, several tasks such as motion segmentation [13], and soiling detection [14] were demonstrated on fisheye images without rectification.

In our previous article, *FisheyeDistanceNet* [1], we introduced the first end-to-end scale-aware, a self-supervised monocular training method for fisheye cameras with a large view to regress a Euclidean distance map. In this work, we generalize the training framework to work with any camera model and propose a fully-differentiable architecture that estimates the depth directly from raw unrectified images (shown in Fig. 3) without the need for any pre-processing. In terms of the motivation of a generic training framework, the closest related work is CAM-Convs [15], where authors propose a generic training framework for different types of cameras. However, they do not handle non-linear distortion, and it is not a self-supervised method. Our contributions include:

¹<https://youtu.be/K6pbx3bU4Ss>

- A generic end-to-end novel self-supervised training pipeline to estimate monocular depth estimation on raw distorted images from various camera models.
- Empirical evaluation of two diverse automotive datasets, namely KITTI and WoodScape.
- First demonstration of depth estimation results directly on unrectified KITTI sequences.
- State of the art results on KITTI depth estimation among self-supervised methods.
- In our generic framework, we propose a simple solution to the scale factor uncertainty with support from odometry data, allowing to output metric depth maps.

II. MOTIVATION FOR WORKING ON RAW IMAGES

Distortion in Automotive Cameras: To handle the wide variety of automotive use cases, different cameras having a different field of view are used. The most common ones are around 100° hFOV (horizontal field of view) cameras used for front camera sensing and 190° hFOV fisheye lens cameras for surround-view sensing. Due to their moderate to large FOV, these cameras suffer from lens distortion, whose main component is typically radial distortion and minor tangential distortion.

Moderate FOV Lens Models: For lenses with a moderate FOV ($< 120^\circ$), Brown-Conrady model [16] is commonly used as it models both radial and tangential distortion. For higher FOV, this distortion model typically breaks down or requires very high polynomial orders. The KITTI dataset's calibration uses this model based on OpenCV's implementation. In this model, the projection function $X_c \mapsto \Pi(X_c) = p$ maps a 3D point $X_c = (x_c, y_c, z_c)^T$ in camera coordinates to a pixel $p = (u, v)^T$ in the image coordinates. It is calculated in the following way:

$$\begin{aligned} x &= x_c/z_c, \quad y = y_c/z_c \\ x' &= x(1 + k_1r^2 + k_2r^4 + k_3r^6) + 2p_1xy + p_2(r^2 + 2x^2) \\ y' &= y(1 + k_1r^2 + k_2r^4 + k_3r^6) + p_1(r^2 + 2y^2) + 2p_2xy \\ u &= f_x \cdot x' + c_x, \quad v = f_y \cdot y' + c_y \end{aligned}$$

where k_1 , k_2 , and k_3 are radial distortion coefficients, p_1 and p_2 are tangential distortion coefficients of the lens, $r^2 = x^2 + y^2$, f_x , f_y are the focal lengths and c_x , c_y are the coordinates of the principal point.

Fisheye Lens Models: For fisheye lenses, the mapping of 3D points to pixels universally requires a radial component $r(\theta)$ [17]. The projection is a complex multi-stage process compared to regular lenses and thus we list the detailed steps:

- 1) The point X_c in camera coordinates is mapped to a unit vector as $S = (s_x, s_y, s_z)^T = X_c/\|X_c\|$.
- 2) The incident angle against the optical axis (coincident with the Z -axis) $\theta = \frac{\pi}{2} - \arcsin(s_z)$ is computed.
- 3) The radial function $r(\theta)$ to get the radius on the image plane (typically in pixels) is computed.
- 4) Given the pixel distortion centre (c_x, c_y) , the pixel location is given by $u = r \cdot s_x + c_x$ and $v = r \cdot s_y + c_y$.
- 5) (optional) Depending on the model used in Step 3, an additional distortion correction may need to be applied.



Fig. 2 **Illustration of distortion correction in KITTI and WoodScape datasets.** The first row shows a raw KITTI image with barrel distortion and the corresponding rectified image. The red box was used to crop out black pixels in periphery causing a loss of FOV. The second row shows a raw WoodScape image with strong fisheye lens distortion and the corresponding rectified image causing a drastic loss of FOV.

We discuss the projection models which are supported in our framework. The polynomial model is the commonly used (and relatively recent projection models are UCM (Unified Camera Model) [18] and eUCM (Enhanced UCM) [19]. Rectilinear (representation of pinhole model) and Stereographic (mapping of sphere to a plane) are not suitable for fisheye lenses but provided for comparison. Double Sphere [20] is a recently proposed model which has a closed form inverse with low computational complexity. The radial distortion models are summarized below:

- 1) Polynomial: $r(\theta) = a_1\theta + a_2\theta^2 + a_3\theta^3 + a_4\theta^4$
- 2) UCM: $r(\theta) = f \cdot \sin(\theta)/(\cos(\theta) + \xi)$
- 3) eUCM: $r(\theta) = f \cdot \frac{\sin(\theta)}{\cos(\theta) + \alpha(\sqrt{\beta \cdot \sin(\theta)^2 + \cos(\theta)^2} - \cos(\theta))}$
- 4) Rectilinear: $r(\theta) = f \cdot \tan(\theta)$
- 5) Stereographic: $r(\theta) = 2f \cdot \tan(\theta/2)$

Practical Problems encountered: In the previous subsection, we have established that real-world automotive cameras have lens distortion. The typical approach is to remove the distortion and then apply standard models. However, in practice, this has several issues that are not dealt with in the literature. Fig. 2 illustrates the rectification used in KITTI and WoodScape datasets. In the KITTI dataset, due to the barrel² distortion effect of the camera, images have been rectified and cropped to 1242×375 pixels. Cropping is performed after rectification to get a rectangular grid without any black pixels in the periphery. Thus the size of the rectified images is smaller than that of the raw images with 1392×512 pixels. Based on the number of the non-black, occupied pixels removed by the cropping, roughly 10% of the image, information is lost. This effect becomes more drastic for the WoodScape images with a much larger radial distortion were more than 30% of the image, information is lost³. For a horizontal FOV greater than 180° , there are rays incidents from behind the camera, making it theoretically impossible to establish a complete mapping to a rectilinear viewport. Thus the rectification defeats the purpose of using a wide-

²KITTI [21] refers to it as pincushion distortion because of an error in the OpenCV documentation which was fixed later.

³Other quasi-linear rectification methods like cylindrical rectification will preserve more information at the cost of additional distortion.

angle fisheye lens.

Reduced FOV is the most critical problem of undistortion, but there are further practical issues. The first one is resampling distortion, which is caused by interpolation errors during the warping step. This effect can be partially mitigated by a more advanced interpolation method [22]. However, it is particularly high in the periphery of fisheye lenses because a small region is expanded to a larger one in the warped image. Besides, the warping step is needed at inference time, which consumes significant computing power and memory bandwidth.

The other issue is related to calibration. In an industrial setup, millions of cameras are deployed, and they have manufacturing variations. The camera parameters (mainly focal length) can also vary due to high ambient temperatures when driving in a hot region. Thus a model that relies on rectification to correct the distortion could have errors. For instance, dataset capture and training are typically performed on one particular camera, and the model is deployed to work on millions of cameras in commercial vehicles. Thus rectification and cropping to a standard resolution as per the training camera are sub-optimal for a deployed camera. However, when CNN learns the distortion as part of the transfer function, it is only weakly encoded and thus expected to be more robust. To alleviate these issues, we are motivated to explore a depth estimation model that can work directly on raw images without needing rectification.

III. SELF-SUPERVISED SCALE-AWARE DEPTH ESTIMATION

Following Zhou *et al.* [4] we aim at learning a self-supervised monocular structure-from-motion (SfM):

- 1) a scale-ambiguous depth \hat{D} is obtained through a self-supervised monocular model $g_D : I_t \rightarrow D$ outputting $\hat{D} = g_D(I_t(p))$ per pixel p in the target image I_t ; and
- 2) Rigid transformations from $T_{t \rightarrow t'} \in \text{SE}(3)$ which predicts a set of 6 degrees of freedom is estimated using an ego-motion predictor $g_x : (I_t, I_{t'}) \rightarrow I_{t \rightarrow t'}$, between the target image I_t and the set of reference images $I_{t'}$. Generally, $t' \in \{t+1, t-1\}$, i.e. the frames I_{t-1} and I_{t+1} are used as reference images, but it is possible to use a larger offset from the temporal consistent sequence.

In all the previous works [4], [3], [23], networks are equipped to retrieve inverse depth $g_d : p \mapsto g_D^{-1}(I_t(p))$. One downside to these methods is the scale ambiguity in both depth and pose estimation. In this work, we recover scale-aware depth directly for distorted images. View-synthesis is used as a self-supervising technique, and the network is trained with the source images I_{t-1} and I_{t+1} to synthesize the appearance of a target image I_t . For this, we need the projection function Π of the chosen camera model, which maps a 3D point X_c in camera coordinates to a pixel $p = \Pi(X_c)$ in image coordinates. An overview of projection models for different lens types can be found in Section II. The corresponding unprojection function Π^{-1} , which maps an image pixel p and its depth estimate \hat{D} to the 3D

point $X_c = \Pi^{-1}(p, \hat{D})$, is also required. If Π^{-1} cannot be expressed in analytic form, a pre-calculated lookup table is used to ensure computational efficiency.

View Synthesis for Various Camera Models: Consider the image reconstruction error of $I_{t'}$ and I_t pair of frames, the depth estimate \hat{D}_t at time t . Using the network's \hat{D}_t depth estimate a point cloud P_t is obtained through:

$$P_t = \Pi^{-1}(p_t, \hat{D}_t) \quad (1)$$

The unprojection from image to camera coordinates is represented by Π^{-1} , the pixel set of image I_t by p_t . The pose relative to I_t corresponding to the source image $I_{t'}$'s pose, is considered as $T_{t \rightarrow t'}$. For point cloud of the image $I_{t'}$ an estimate $\hat{P}_{t'} = T_{t \rightarrow t'} P_t$ is obtained by the pose network's estimate $T_{t \rightarrow t'}$. The projection model Π is used at time t' to project $\hat{P}_{t'}$ onto the pinhole camera. The projection and transformation are combined with Eq. 1 to establish a mapping $p_t = (i, j)^T$ at time t from image coordinates to $\hat{p}_{t'} = (i, j)^T$ at time t' . View synthesised image $\hat{I}_{t' \rightarrow t}$ of the target frame I_t is computed using this mapping by backward warping the source frame $I_{t'}$.

$$\hat{p}_{t'} = \Pi(T_{t \rightarrow t'} \Pi^{-1}(p_t, \hat{D}_t)), \quad \hat{I}_{t' \rightarrow t}^{ij} = \langle \hat{I}_{t'}^{ij} \rangle \quad (2)$$

Because the warped coordinates \hat{i}, \hat{j} are continuous, differentiable spatial transformer network [24] can be used to synthesize $\hat{I}_{t' \rightarrow t}$ by bilinear interpolation of the four pixels of $I_{t'}$ close $\hat{p}_{t'}$. The $\langle \dots \rangle$ symbol denotes the corresponding sample operator.

Reconstruction Loss: The L1 pixel-wise loss is coupled with Structural Similarity (SSIM) [25], to form an image reconstruction loss \mathcal{L}_r between the target image I_t and the reconstructed target image $\hat{I}_{t' \rightarrow t}$ and is given by Eq. 3 below.

$$\begin{aligned} \tilde{\mathcal{L}}_r(I_t, \hat{I}_{t' \rightarrow t}) &= \omega \frac{1 - \text{SSIM}(I_t, \hat{I}_{t' \rightarrow t}, \mathcal{M}_{t \rightarrow t'})}{2} \\ &\quad + (1 - \omega) \left\| (I_t - \hat{I}_{t' \rightarrow t}) \odot \mathcal{M}_{t \rightarrow t'} \right\|_1 \\ \mathcal{L}_r &= \min_{t' \in \{t+1, t-1\}} \tilde{\mathcal{L}}_r(I_t, \hat{I}_{t' \rightarrow t}) \end{aligned} \quad (3)$$

The binary mask $\mathcal{M}_{t \rightarrow t'}$ is incorporated from [1], element-wise multiplication is denoted by \odot and ω is set to 0.85. Following [3], we adopt a per-pixel minimum compared to averaging over all the source images. It yields higher accuracy by reducing the artifacts and significantly sharpens the boundaries of occlusion. We clip the reconstruction loss values to a 95th percentile-based on [26] to diminish the impact of dynamic objects or occluded areas in the scene. It indirectly aids the optimization algorithm to have a robust reconstruction error.

Solving Scale Factor Ambiguity at Training Time: The network's sigmoid output σ can be translated to depth with $D = 1/(x\sigma + y)$, where x and y are chosen to constrain D between 0.1 and 100 units [3] based on the fact that $depth \propto 1/disparity$ for a rectified pinhole projection model. We can only obtain angular disparities [27] for

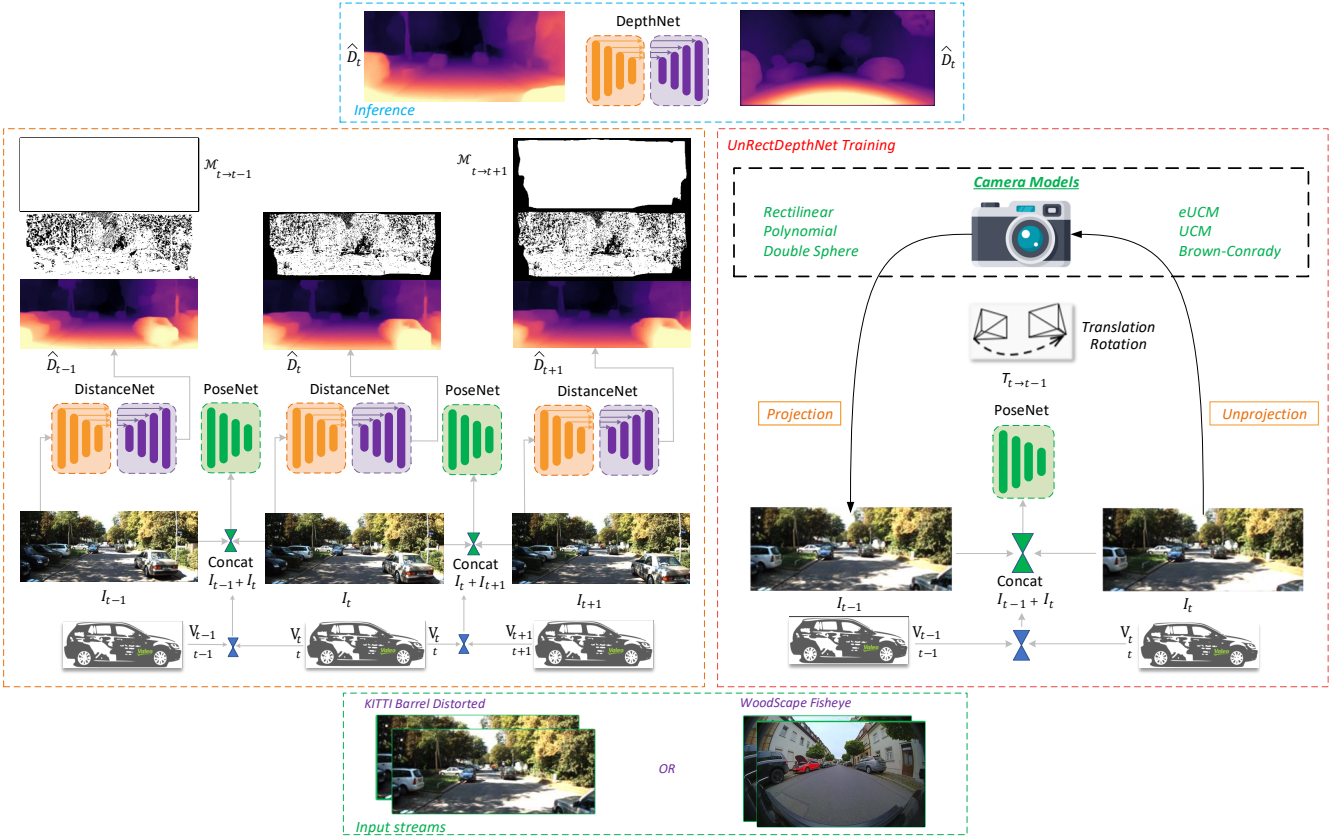


Fig. 3: **Overview of our generic depth estimation training framework UnRectDepthNet.** The UnRectDepthNet training block on the right enables the usage of various camera models generically listed in the black box. The distortion is then handled internally in the unprojection and projection steps of the transformation from $I_{t \rightarrow t-1}$. In this paper, we have tested it with KITTI barrel distorted and WoodScape fisheye distorted video sequences. The block on the left indicates the entire workflow of the training pipeline where the top row depicts the ego-masks as explained in [1], $\mathcal{M}_{t \rightarrow t-1}$, $\mathcal{M}_{t \rightarrow t+1}$ valid pixel coordinates while synthesizing $\hat{I}_{t-1 \rightarrow t}$ from I_{t-1} and $\hat{I}_{t+1 \rightarrow t}$ from I_{t+1} respectively. The following row showcases the masks used to filter static pixels, obtained after training two epochs, and the black pixels are removed from the reconstruction loss. The dynamic objects moving at speed similar to the ego-car, and also, the homogeneous areas are filtered to prevent the contamination of reconstruction loss. The third row indicates the depth predictions, and the scale-ambiguity is resolved using the ego vehicle’s odometry data. Finally, the top block illustrates the inference output on distorted images.

camera models which undergo distortion. To perform a successful inverse warp operation of source images $I_{t'}$ onto the target frame I_t on camera models which undergo distortion, metric depth values are required. *Scale-ambiguous* estimates from both the g_d monocular depth model and the g_x ego-motion predictor make it difficult to predict depth maps on any model of choice because of the inherent drawback of the self-supervised structure-from-motion objective. Following [1], we solve the scale ambiguity, by normalizing the pose network’s prediction $T_{t \rightarrow t'}$ to obtain scale-aware depth values. We compute the displacement magnitude Δx relative to target frame I_t utilizing the ego-vehicle’s instantaneous velocity predictions $v_{t'}$ at time t' and v_t at time t obtained from the ego-vehicle’s odometry data. Finally, we scale the normalized translation vector with Δx . The same method is also incorporated on KITTI [21] rectified pinhole dataset to achieve scale-aware depth maps.

$$\bar{T}_{t \rightarrow t'} = \frac{T_{t \rightarrow t'}}{\|T_{t \rightarrow t'}\|} \cdot \Delta x \quad (4)$$

Edge-Aware Depth Smoothness Loss: A geometric smoothness loss is added to regularize depth and avoid different values in occluded or homogeneous areas. We incorporate the edge-aware loss term and impose it on the inverse depth map term similar to [5], [28], [29].

$$\mathcal{L}_s(\hat{D}_t) = |\partial_u \hat{D}_t^*| e^{-|\partial_u I_t|} + |\partial_v \hat{D}_t^*| e^{-|\partial_v I_t|} \quad (5)$$

Following [6], mean-normalized inverse depth \hat{D}_t^* of the target image I_t is considered to avoid any shrinkage of depth estimates \hat{D}_t , i.e. $\hat{D}_t^* = \hat{D}_t^{-1} / \bar{D}_t$, where \bar{D}_t denotes the mean of $\hat{D}_t^{-1} := 1 / \hat{D}_t$.

Final Training Loss: The final self-supervised structure-from-motion (SfM) *from motion* objective comprises of a reconstruction loss \mathcal{L}_r applied on forward and backward sequences and an edge-aware smoothness term \mathcal{L}_s to regularize depth. Finally, \mathcal{L}_{dc} a cross-sequence depth consistency loss estimated from the sequence of frames in the training videos S is also incorporated from [1]. As the bilinear sampler has gradient locality [24], we include four scales for training as suggested in [4], [5] mainly to reduce the chances of training

| Method | Resolution | Dataset | Abs Rel | Sq Rel | RMSE | RMSE _{log} | $\delta < 1.25$ | | | $\delta < 1.25^2$ | | $\delta < 1.25^3$ | |
|---------------|------------------------|------------|---------|--------------|--------------|---------------------|-----------------|--------------|--------------|-------------------|--|-------------------|--|
| | | | | | | | lower is better | | | higher is better | | | |
| Original [30] | SfMLearner [4] | 416 x 128 | K | 0.183 | 1.595 | 6.709 | 0.270 | 0.734 | 0.902 | 0.959 | | | |
| | Vid2depth [28] | 416 x 128 | K | 0.163 | 1.240 | 6.220 | 0.250 | 0.762 | 0.916 | 0.968 | | | |
| | DDVO [6] | 416 x 128 | K | 0.151 | 1.257 | 5.583 | 0.228 | 0.810 | 0.936 | 0.974 | | | |
| | EPC++ [31] | 640 x 192 | K | 0.141 | 1.029 | 5.350 | 0.216 | 0.816 | 0.941 | 0.976 | | | |
| | Struct2Depth [32] | 416 x 128 | K | 0.141 | 1.026 | 5.291 | 0.215 | 0.816 | 0.945 | 0.979 | | | |
| | Monodepth2 [3] | 640 x 192 | K | 0.115 | 0.903 | 4.863 | 0.193 | 0.877 | 0.959 | 0.981 | | | |
| | PackNet-SfM [23] | 640 x 192 | K | 0.111 | 0.785 | 4.601 | 0.189 | 0.878 | 0.960 | 0.982 | | | |
| Improved [33] | Monodepth2 [3] | 1024 x 320 | K | 0.115 | 0.882 | 4.701 | 0.190 | 0.879 | 0.961 | 0.982 | | | |
| | UnRectDepthNet | 640 x 192 | K | 0.107 | 0.721 | 4.564 | 0.178 | 0.894 | 0.971 | 0.986 | | | |
| | UnRectDepthNet | 1024 x 320 | K | 0.103 | 0.705 | 4.386 | 0.164 | 0.897 | 0.980 | 0.989 | | | |
| | UnRectDepthNet | 608 x 224 | KD | 0.102 | 0.720 | 4.559 | 0.183 | 0.892 | 0.973 | 0.988 | | | |
| | UnRectDepthNet | 1216 x 448 | KD | 0.106 | 0.709 | 4.357 | 0.161 | 0.895 | 0.984 | 0.992 | | | |
| | FisheyeDistanceNet [1] | 512 x 256 | WS | 0.152 | 0.768 | 2.723 | 0.210 | 0.812 | 0.954 | 0.974 | | | |
| | UnRectDepthNet | 512 x 256 | WS | 0.148 | 0.702 | 2.530 | 0.212 | 0.826 | 0.960 | 0.980 | | | |
| Original [30] | SfMLearner [4] | 416 x 128 | K | 0.176 | 1.532 | 6.129 | 0.244 | 0.758 | 0.921 | 0.971 | | | |
| | Vid2Depth [28] | 416 x 128 | K | 0.134 | 0.983 | 5.501 | 0.203 | 0.827 | 0.944 | 0.981 | | | |
| | DDVO [6] | 416 x 128 | K | 0.126 | 0.866 | 4.932 | 0.185 | 0.851 | 0.958 | 0.986 | | | |
| | EPC++ [31] | 640 x 192 | K | 0.120 | 0.789 | 4.755 | 0.177 | 0.856 | 0.961 | 0.987 | | | |
| | Monodepth2 [3] | 640 x 192 | K | 0.090 | 0.545 | 3.942 | 0.137 | 0.914 | 0.983 | 0.995 | | | |
| | PackNet-SfM [23] | 640 x 192 | K | 0.078 | 0.420 | 3.485 | 0.121 | 0.931 | 0.986 | 0.996 | | | |
| | UnRectDepthNet | 640 x 192 | K | 0.081 | 0.414 | 3.412 | 0.117 | 0.926 | 0.987 | 0.996 | | | |
| Improved [33] | UnRectDepthNet | 640 x 224 | KD | 0.092 | 0.458 | 3.503 | 0.132 | 0.906 | 0.971 | 0.990 | | | |

TABLE I: **Quantitative performance comparison of UnRectDepthNet** for depths up to 80 m for KITTI and 40 m for FisheyeDistanceNet. In the Dataset column, K refers to KITTI [34], KD refers to the Kitti Distorted [34], and WS refers to WoodScape [1] dataset. *Original* refers to depth maps defined in [30], and *Improved* refers to refined depth maps provided by [33]. All the methods listed in the table are self-supervised approaches on monocular camera sequences. At inference time, all the approaches except UnRectDepthNet and PackNet-SfM, scale the estimated depths using median ground-truth LiDAR depth. We generalized our previous model FisheyeDistanceNet in our new training framework and added additional features which improved results in WoodScape [35] marked as WS.

| Method | FS | BS | SR | CSDCL | Abs Rel | Sq Rel | RMSE | RMSE log | $\delta < 1.25$ | $\delta < 1.25^2$ | $\delta < 1.25^3$ |
|--------|----|----|----|-------|---------|--------|-------|----------|-----------------|-------------------|-------------------|
| Ours | ✓ | ✓ | ✓ | ✓ | 0.102 | 0.720 | 4.559 | 0.183 | 0.892 | 0.973 | 0.988 |
| Ours | ✓ | | ✓ | ✓ | 0.131 | 0.856 | 4.933 | 0.198 | 0.853 | 0.954 | 0.968 |
| Ours | ✓ | | | ✓ | 0.141 | 0.971 | 5.183 | 0.206 | 0.831 | 0.941 | 0.953 |
| Ours | ✓ | | | | 0.144 | 1.011 | 5.204 | 0.225 | 0.822 | 0.945 | 0.949 |

TABLE II: **Ablation study of our algorithm** on the KITTI Eigen split dataset [21]. Depths are capped at 80 m. FS, BS, SR (ICNR), CSDCL indicate forward sequence, backward sequence, super-resolution network with PixelShuffle [36] layers and cross-sequence depth consistency loss, respectively. The input resolution is 608 x 224 pixels.

reaching a local minima. The overall objective function is averaged over the number of pixels, scales and batches.

$$\mathcal{L} = \sum_{n=1}^4 \frac{\mathcal{L}_n}{2^{n-1}}, \quad (6)$$

$$\mathcal{L}_n = {}^n\mathcal{L}_r^f + {}^n\mathcal{L}_r^b + \gamma {}^n\mathcal{L}_{dc} + \beta {}^n\mathcal{L}_s$$

IV. IMPLEMENTATION DETAILS

The depth estimation network is mainly based on FisheyeDistanceNet [1]. We use Pytorch [37] and employ Ranger (RAdam [38] + LookAhead [39]) optimizer to minimize the training objective function (6). The model is trained using Titan RTX with a batch size of 20 for 20 epochs, with initial learning rate of 4×10^{-4} with OneCycleScheduler [40]. The network’s sigmoid output σ is converted to depth with $D = 1/(x \cdot \sigma + y)$ for pinhole model and $D = x \cdot \sigma + y$ for fisheye, where x and y is chosen to constrain D between 0.1 and 100 units. For KITTI distorted images, we use 608 x 224 pixels, and for fisheye 512 x 256 pixels as the network input to maintain the original aspect ratio. The loss weightage factors β and γ of smoothness and cross-sequence depth consistency loss are set

to 0.001. To remove checkerboard artifacts in the sub-pixel convolution [41], the final convolutional layers are initialized in a particular manner before the pixel shuffle operation as described in [36].

V. EXPERIMENTS

Datasets – KITTI and WoodScape: For experiments with the pinhole camera model, the KITTI dataset is used as per the split defined in Eigen et al. [42]. Following Zhou et al. [4], the static frames are dropped from the dataset. There are 39,810 images for training, 4,424 images for validation, and 697 images for testing. We also make use of the 652 improved ground truth of the Eigen split test frames provided by [33]. The WoodScape [35] dataset distribution can be found in our FisheyeDistanceNet [1].

Evaluation: To facilitate the comparison, we evaluate the results of UnRectDepthNet depth estimation using the metrics proposed by Eigen et al. [30]. Table I indicates the quantitative results. It illustrates that our scale-aware self-supervised approach on KITTI rectified outperforms all the state-of-the-art monocular approaches and the KITTI Distorted results are better than most of the previous self-

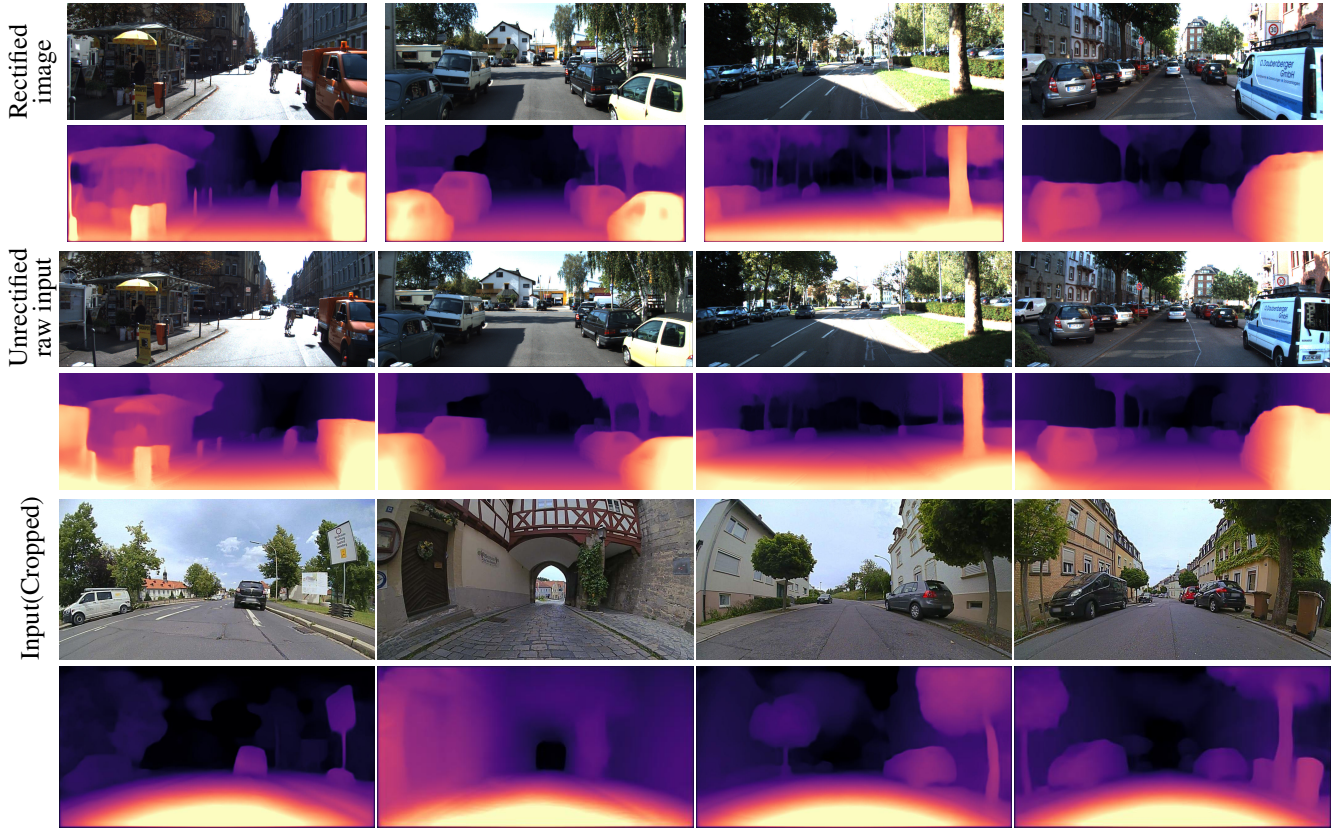


Fig. 4: Qualitative result comparison on KITTI unrectified and WoodScape dataset. The results on a distorted test scene video sequence indicate excellent performance which can be viewed with the link: [UnRectDepthNet](#)

supervised approaches on KITTI rectified dataset. Owing to the absence of odometry data the Cityscapes dataset is not leveraged into our training framework.

Because the projection’s operators are different, prior approaches to depth estimation will not work on the WoodScape fisheye dataset without significant redesign to incorporate fisheye projection geometry. In addition, fisheye cameras are designed for near-field sensing, and we only compare up to a range of 40 m as per FisheyeDistanceNet [1]. We generalized the training methodology of this model to incorporate any arbitrary distortion model. We also tuned our network to the best optimal hyperparameters using grid search and removed batch normalization in the decoder as we observed ghosting effects and holes in homogenous areas. We calculated minimum reconstruction error in the backward sequences individually compared to combined minimization in forward sequence as the target frame belongs to $I_{t'}$, as explained in Section III.

KITTI Distorted Ablation Study: We perform an ablation study to understand the significance of different components used and tabulate in Table II: (i) *Remove Backward Sequence*: The network is trained only for a forward sequence consisting of two warps, as explained in [1]. The impact is significant in the border areas as fewer constraints are induced. The model inherently fails to resolve unknown distances in those areas at the test time, which can be observed in previous works [3], [4], [43]; (ii) *Additionally remove Super-Resolution using sub-pixel convolution*: It has

a significant effect as distant objects are small in fisheye cameras and can not be resolved correctly with simple nearest-neighbor interpolation or transposed convolution [44]; (iii) *Additionally remove cross-sequence depth consistency loss*: The removal of the CSDCL diminishes the baseline, induces fewer constraints, and the model is not robust to yield accurate distance estimates.

VI. CONCLUSION

We introduced a generic self-supervised training method for depth estimation handling distorted images. We support various commonly used automotive camera models in the framework and indicate empirical results on KITTI and WoodScape datasets. In KITTI, we show that depth estimation of unrectified images can produce the same accuracy as rectified images. We also obtain a state of the art results on KITTI among self-supervised algorithms. The same framework was used to train fisheye unrectified images in the WoodScape dataset, where only the corresponding camera model parameters were updated. In future work, we aim to extend the training framework to take in various camera streams as input and output a generic inference model which can take in camera model as an argument.

Acknowledgements: We want to thank Valeo, especially DAR Kronach, Germany and Valeo Vision Systems, Ireland for supporting the creation of the WoodScape dataset. We want to thank Ciarán Eising (Valeo) and Ravi Kiran (Navya) for providing a detailed review.

REFERENCES

[1] V. R. Kumar, S. A. Hiremath, S. Milz, C. Witt, C. Pinnard, S. Yogamani, and P. Mader, "Fisheyedistance: Self-supervised scale-aware distance estimation using monocular fisheye camera for autonomous driving," *arXiv preprint arXiv:1910.04076*, 2019.

[2] U. Franke, D. Gavrila, S. Gorzig, F. Lindner, F. Puetzold, and C. Wohler, "Autonomous driving goes downtown," *IEEE Intelligent Systems and Their Applications*, vol. 13, no. 6, pp. 40–48, 1998.

[3] C. Godard, O. Mac Aodha, M. Firman, and G. J. Brostow, "Digging into self-supervised monocular depth estimation," in *Proceedings of the IEEE international conference on computer vision*, 2019, pp. 3828–3838.

[4] T. Zhou, M. Brown, N. Snavely, and D. G. Lowe, "Unsupervised learning of depth and ego-motion from video," in *Proceedings of the IEEE Conference on Computer Vision and Pattern Recognition*, 2017, pp. 1851–1858.

[5] C. Godard, O. Mac Aodha, and G. J. Brostow, "Unsupervised monocular depth estimation with left-right consistency," in *CVPR*, 2017.

[6] C. Wang, J. Buenaposada, R. Zhu, and S. Lucey, "Learning depth from monocular videos using direct methods," in *The IEEE Conference on Computer Vision and Pattern Recognition (CVPR)*, June 2018.

[7] V. Ravi Kumar, S. Milz, C. Witt, M. Simon, K. Amende, J. Petzold, S. Yogamani, and T. Pech, "Monocular fisheye camera depth estimation using sparse lidar supervision," in *2018 21st International Conference on Intelligent Transportation Systems (ITSC)*. IEEE, 2018, pp. 2853–2858.

[8] G. Sistu, I. Leang, S. Chennupati, S. Yogamani, C. Hughes, S. Milz, and S. Rawashdeh, "Neural: Towards a unified visual perception model for automated driving," in *2019 IEEE Intelligent Transportation Systems Conference (ITSC)*. IEEE, 2019, pp. 796–803.

[9] S. Chennupati, G. Sistu, S. Yogamani, and S. A Rawashdeh, "Multi-net++: Multi-stream feature aggregation and geometric loss strategy for multi-task learning," in *Proceedings of the IEEE Conference on Computer Vision and Pattern Recognition Workshops*, 2019, pp. 0–0.

[10] S. Chennupati, G. Sistu, S. Yogamani, and S. Rawashdeh, "Auxnet: Auxiliary tasks enhanced semantic segmentation for automated driving," in *Proceedings of the 14th International Joint Conference on Computer Vision, Imaging and Computer Graphics Theory and Applications - Volume 5: VISAPP*, INSTICC. SciTePress, 2019, pp. 645–652.

[11] R. Hartley and A. Zisserman, *Multiple view geometry in computer vision*. Cambridge university press, 2003.

[12] P. Yadati and A. M. Namboodiri, "Multiscale two-view stereo using convolutional neural networks for unrectified images," in *2017 Fifteenth IAPR International Conference on Machine Vision Applications (MVA)*. IEEE, 2017, pp. 346–349.

[13] M. Yahiaoui, H. Rashed, L. Mariotti, G. Sistu, I. Clancy, L. Yahiaoui, V. R. Kumar, and S. Yogamani, "Fisheyemodnet: Moving object detection on surround-view cameras for autonomous driving," *arXiv preprint arXiv:1908.11789*, 2019.

[14] M. Uříčák, P. Křížek, G. Sistu, and S. Yogamani, "Soilingnet: Soiling detection on automotive surround-view cameras," in *2019 IEEE Intelligent Transportation Systems Conference (ITSC)*. IEEE, 2019.

[15] J. M. Facil, B. Ummenhofer, H. Zhou, L. Montesano, T. Brox, and J. Civera, "Cam-convs: camera-aware multi-scale convolutions for single-view depth," in *Proceedings of the IEEE conference on computer vision and pattern recognition*, 2019, pp. 11 826–11 835.

[16] A. E. Conrady, "Decentred lens-systems," *Monthly notices of the royal astronomical society*, vol. 79, no. 5, pp. 384–390, 1919.

[17] C. Hughes, P. Denny, E. Jones, and M. Glavin, "Accuracy of fish-eye lens models," *Applied Optics*, vol. 49, no. 17, pp. 3338–3347, 2010.

[18] J. P. Barreto, "Unifying image plane liftings for central catadioptric and dioptric cameras," *Imaging Beyond the Pinhole Camera*, 2006.

[19] B. Khomutenko, G. Garcia, and P. Martinet, "An enhanced unified camera model," *IEEE Robotics and Automation Letters*, vol. 1, no. 1, pp. 137–144, 2016.

[20] V. Usenko, N. Demmel, and D. Cremers, "The double sphere camera model," in *2018 International Conference on 3D Vision (3DV)*. IEEE, 2018, pp. 552–560.

[21] A. Geiger, P. Lenz, C. Stiller, and R. Urtasun, "Vision meets robotics: The kitti dataset," *The International Journal of Robotics Research*, vol. 32, no. 11, pp. 1231–1237, 2013.

[22] E. Meijering, "A chronology of interpolation: from ancient astronomy to modern signal and image processing," *Proceedings of the IEEE*, vol. 90, no. 3, pp. 319–342, 2002.

[23] V. Guizilini, R. Ambrus, S. Pillai, A. Raventos, and A. Gaidon, "3d packing for self-supervised monocular depth estimation," in *IEEE Conference on Computer Vision and Pattern Recognition (CVPR)*, 2020.

[24] M. Jaderberg, K. Simonyan, A. Zisserman, *et al.*, "Spatial transformer networks," in *Advances in neural information processing systems*, 2015, pp. 2017–2025.

[25] Z. Wang, A. C. Bovik, H. R. Sheikh, E. P. Simoncelli, *et al.*, "Image quality assessment: from error visibility to structural similarity," *IEEE transactions on image processing*, vol. 13, no. 4, pp. 600–612, 2004.

[26] L. Zhou, J. Ye, M. Abello, S. Wang, and M. Kaess, "Unsupervised learning of monocular depth estimation with bundle adjustment, super-resolution and clip loss," *arXiv preprint arXiv:1812.03368*, 2018.

[27] Z. Arican and P. Frossard, "Dense depth estimation from omnidirectional images," 2009.

[28] R. Mahjourian, M. Wicke, and A. Angelova, "Unsupervised learning of depth and ego-motion from monocular video using 3d geometric constraints," in *Proceedings of the IEEE Conference on Computer Vision and Pattern Recognition*, 2018, pp. 5667–5675.

[29] Y. Zou, Z. Luo, and J.-B. Huang, "Df-net: Unsupervised joint learning of depth and flow using cross-task consistency," in *Proceedings of the European Conference on Computer Vision (ECCV)*, 2018, pp. 36–53.

[30] D. Eigen, C. Puhrsch, and R. Fergus, "Depth map prediction from a single image using a multi-scale deep network," in *Advances in neural information processing systems*, 2014, pp. 2366–2374.

[31] C. Luo, Z. Yang, P. Wang, Y. Wang, W. Xu, R. Nevatia, and A. Yuille, "Every pixel counts++: Joint learning of geometry and motion with 3d holistic understanding," *arXiv preprint arXiv:1810.06125*, 2018.

[32] V. Casser, S. Pirk, R. Mahjourian, and A. Angelova, "Depth prediction without the sensors: Leveraging structure for unsupervised learning from monocular videos," in *Proceedings of the AAAI Conference on Artificial Intelligence*, vol. 33, 2019, pp. 8001–8008.

[33] J. Uhrig, N. Schneider, L. Schneider, U. Franke, T. Brox, and A. Geiger, "Sparsity invariant cnns," in *2017 International Conference on 3D Vision (3DV)*. IEEE, 2017, pp. 11–20.

[34] A. Geiger, "Are we ready for autonomous driving? the kitti vision benchmark suite," in *Proceedings of the 2012 IEEE Conference on Computer Vision and Pattern Recognition (CVPR)*, ser. CVPR '12. Washington, DC, USA: IEEE Computer Society, 2012, pp. 3354–3361.

[35] S. Yogamani, C. Hughes, J. Horgan, G. Sistu, P. Varley, D. O'Dea, M. Uricár, S. Milz, M. Simon, K. Amende, *et al.*, "Woodscape: A multi-task, multi-camera fisheye dataset for autonomous driving," in *Proceedings of the IEEE International Conference on Computer Vision*, 2019, pp. 9308–9318.

[36] A. Aitken, C. Ledig, L. Theis, J. Caballero, Z. Wang, and W. Shi, "Checkerboard artifact free sub-pixel convolution: A note on sub-pixel convolution, resize convolution and convolution resize," *arXiv preprint arXiv:1707.02937*, 2017.

[37] A. Paszke, S. Gross, S. Chintala, G. Chanan, E. Yang, Z. DeVito, Z. Lin, A. Desmaison, L. Antiga, and A. Lerer, "Automatic differentiation in PyTorch," in *NIPS Autodiff Workshop*, 2017.

[38] L. Liu, H. Jiang, P. He, W. Chen, X. Liu, J. Gao, and J. Han, "On the variance of the adaptive learning rate and beyond," *arXiv preprint arXiv:1908.03265*, 2019.

[39] M. Zhang, J. Lucas, J. Ba, and G. E. Hinton, "Lookahead optimizer: k steps forward, 1 step back," in *Advances in Neural Information Processing Systems*, 2019, pp. 9593–9604.

[40] L. N. Smith and N. Topin, "Super-convergence: Very fast training of neural networks using large learning rates," in *Artificial Intelligence and Machine Learning for Multi-Domain Operations Applications*, vol. 11006. International Society for Optics and Photonics, 2019.

[41] W. Shi, J. Caballero, F. Huszár, J. Totz, A. P. Aitken, R. Bishop, D. Rueckert, and Z. Wang, "Real-time single image and video super-resolution using an efficient sub-pixel convolutional neural network," in *Proceedings of the IEEE conference on computer vision and pattern recognition*, 2016, pp. 1874–1883.

[42] D. Eigen and R. Fergus, "Predicting depth, surface normals and semantic labels with a common multi-scale convolutional architecture," in *Proceedings of the IEEE international conference on computer vision*, 2015, pp. 2650–2658.

[43] Z. Yin and J. Shi, "Geonet: Unsupervised learning of dense depth, optical flow and camera pose," in *Proceedings of the IEEE Conference on Computer Vision and Pattern Recognition*, 2018, pp. 1983–1992.

[44] A. Odena, V. Dumoulin, and C. Olah, "Deconvolution and checkerboard artifacts," *Distill*, vol. 1, no. 10, p. e3, 2016.